

Room-temperature formation of slanted nanobelts and vertical wires on low-doped p-type(100) silicon via metal-assisted chemical etching

Xiao-Qing Bao(包晓清), Shu Zhang(张姝), Dehua Xiong(熊德华), and Wei Li(李伟)
Citation: Chin. Phys. B, 2026, 35 (**8**): 088103. DOI: 10.1088/1674-1056/ae1119
http://cpb.iphy.ac.cn; http://iopscience.iop.org/cpb

What follows is a list of articles you may be interested in

Probing the improved stability for high nickel cathode via dual-element modification in lithium-ion

Fengling Chen(陈峰岭), Chaozhi Zeng(曾朝智), Chun Huang(黄淳), Jiannan Lin(林建楠), Yifan Chen(陈一帆), Binbin Dong(董彬彬), Chujun Yin(尹楚君), Siying Tian(田飏莹), Dapeng Sun(孙大鹏), Zhenyu Zhang(张振宇), Hong Li(李泓), and Chaobo Li(李超波)
Chin. Phys. B, 2022, 31 (**7**): 078101. DOI: 10.1088/1674-1056/ac598c

Enhancement of electrochemical performance in lithium-ion battery via tantalum oxide coated nickel-rich cathode materials

Fengling Chen(陈峰岭), Jiannan Lin(林建楠), Yifan Chen(陈一帆), Binbin Dong(董彬彬), Chujun Yin(尹楚君), Siying Tian(田飏莹), Dapeng Sun(孙大鹏), Jing Xie (解婧),Zhenyu Zhang(张振宇), Hong Li(李泓), and Chaobo Li(李超波)
Chin. Phys. B, 2022, 31 (**5**): 058101. DOI: 10.1088/1674-1056/ac4481

Improved performance of back-gate MoS_2 transistors by NH_3-plasma treating high-*k* gate dielectrics

Jian-Ying Chen(陈建颖), Xin-Yuan Zhao(赵心愿), Lu Liu(刘璐), Jing-Ping Xu(徐静平)
Chin. Phys. B, 2019, 28 (**12**): 128101. DOI: 10.1088/1674-1056/ab50fe

Influences of substrate temperature on microstructure and corrosion behavior of APS $Ni_{50}Ti_{25}Al_{25}$ inter-metallic coating

Sh Khandanjou, M Ghoranneviss, Sh Saviz, M Reza Afshar
Chin. Phys. B, 2018, 27 (**2**): 028104. DOI: 10.1088/1674-1056/27/2/028104

Room-temperature formation of slanted nanobelts and vertical wires on low-doped p-type (100) silicon via metal-assisted chemical etching

Xiao-Qing Bao(包晓清)[1,2,†,‡], Shu Zhang(张姝)[1,†], Dehua Xiong(熊德华)[3,†], and Wei Li(李伟)[4]

[1] *School of Integrated Circuits, Nanjing University of Information Science and Technology, Nanjing* 210044, *China*
[2] *Nanzhi Institute of Advanced Optoelectronic Integration Technology, Jiangsu Industrial Technology Research Institute, Nanjing* 211800, *China*
[3] *State Key Laboratory of Silicate Materials for Architectures, Wuhan University of Technology, Wuhan* 430070, *China*
[4] *Department of Mechanical and Aerospace Engineering, Benjamin M Statler College of Engineering and Mineral Resources, West Virginia University, Morgantown, WV* 26506, *USA*

(Received 4 August 2025; revised manuscript received 3 October 2025; accepted manuscript online 9 October 2025)

Despite its applications, metal-assisted chemical etching (MACE) is still not well understood. To elucidate its underlying mechanism, MACE with micron-sized Au mesh was systematically carried out across a wide range of volume ratios R of HF acid to H_2O_2 solution. Slanted wires were observed at room temperature over a broad range of parameters, which contradicts the well-established viewpoint that slantwise etching only occurs at elevated temperatures. Vertical wires only form in a narrow parameter space featuring a low R. The wide variation in observed slant angles indicates that the associated MACE processes do not exhibit a preferred etching direction. The observed R-dependent change of oxygen content in wires and of bubbling phenomena was explained by two competing mechanisms associated with direct and indirect Si dissolution. The high- and low-R regimes are dominated by direct and indirect mechanisms, respectively, whereas in the intermediate regime both mechanisms play an indispensable role. Formation of slanted wires is caused directly by slantwise mesh movement. Although this movement is closely correlated with the direct mechanism, it cannot be fully explained by the mechanism. We hypothesize that hydrogen bubbling-induced flow has the potential to hydrodynamically drive the mesh slantwise and hence can be directly responsible for slanted wire formation. To the best of our knowledge, this work not only reports a relatively novel phenomenon — slanted wire formation by MACE at room temperature — but also provides, for the first time, a comprehensive understanding of its underlying complex mechanism.

Keywords: metal-assisted chemical etching, silicon electrochemistry, metal catalysis, hydrogen bubble

PACS: 81.65.–b, 82.45.Vp, 81.16.Hc, 47.55.dd

DOI: 10.1088/1674-1056/ae1119 **CSTR:** 32038.14.CPB.ae1119

1. Introduction

Interest is continuously growing in Si wire research and development for a broad range of potential applications in photovoltaics, thermoelectrics and photonics as well as renewable energy devices.[1–6] For both theoretical and practical investigations, the ability to precisely control wire geometry and morphology is crucial.[4,5] In particular, the controllability of wire direction, whether vertical or tilted with respect to the sample surface, is of obvious importance, since the slant angle of wires affects not only their size but their optical, electronic and photoelectrochemical properties.[7–11]

The vapor–liquid–solid growth method, a bottom-up approach for micro and nano fabrication, enables the yield of high-quality wires. However, this method faces challenges in controllably fabricating slanted and three-dimensional (3D) structures, and it incurs high costs owing to the requirements for precision equipment, high-purity materials and an ultraclean environment. By contrast, as a top-down approach, metal-assisted chemical etching (MACE) is attractive due to its low cost, ease of operation and high tolerance for facilities, as well as to its strong ability to produce complex 3D structures.[1–4] Based on localized microscopic electrochemical processes, chemical etching of Si with a solution containing HF acid and H_2O_2 is believed to be electrochemical in nature.[12–16] The difference between MACE, electrochemical and photoelectrochemical etching lies mainly in the origin of the electronic holes injected into the semiconductor being etched.[14] In Si electrochemistry and photoelectrochemistry holes are provided by bias and illumination, respectively,[17–19] whereas for MACE the provision of holes is completed by a cathodic reaction $H_2O_2+2H^+ \rightarrow 2H_2O+2h^+$.[12–14] The overall current density available for MACE depends on the H_2O_2 concentration.[8,13] As its Gibbs free energy is negative,[12] this reaction is thermodynamically favored but kinetically hindered, thus acting as a rate-limiting step.[12] Hence the use of catalysts is necessary for increasing the current density by lowering the activation energy, as suggested by the Arrhenius equation.[14]

[†]These authors contributed equally to this study.
[‡]Corresponding author. E-mail: 003623@nuist.edu.cn

© 2026 Chinese Physical Society and IOP Publishing Ltd. All rights, including for text and data mining, AI training, and similar technologies, are reserved.

As previously mentioned, controlling the slant angle of Si wires is highly valuable for numerous potential applications. The mechanism of formation of slanted Si wires by MACE remains quite controversial, however. For MACE with etchants composed of a solution of HF acid and H_2O_2, it is common to produce vertical wires on (100) Si substrates due to the well-known crystallographic preference. Chemical, electrochemical, and photoelectrochemical etching of Si prefers $\langle 100 \rangle$ directions since (100) planes are the least compact with the fewest Si back bonds to break. This is true because the effective number of back bonds per Si atom for Si(100), Si(110), and Si(111) planes is one, two, and three, respectively.[7] However, there are also some reports, albeit few, on wire formation along non-$\langle 100 \rangle$ directions. Huang *et al*. demonstrated that etching along $\langle 110 \rangle$ and $\langle 111 \rangle$ directions at room temperature is due mainly to a fast oxidation rate driven by a high concentration of oxidant.[14] Kim *et al*. ascribed $\langle 110 \rangle$ and $\langle 111 \rangle$ etching to the collective effect of two factors, an elevated temperature and a high H_2O_2 concentration able to generate sufficient electronic holes.[7,8] Chen *et al*. reported the fabrication of zigzag wires switched between $\langle 111 \rangle$ and $\langle 113 \rangle$ directions and ascribed this phenomenon to some local perturbations and the elevated temperature they used.[21] Another research group also reported the fabrication of zigzag wires that deviated from the $\langle 100 \rangle$ direction, attributing their formation to reaction rate oscillations caused by unstirred etchants.[22] Hymel *et al*. also reported non-$\langle 100 \rangle$ etching by MACE and explained their results by the electric field effect of Schottky barriers.[23] Interestingly, kinked Si nanowires on Si(100) wafers were also reported, and each kinked part of the wires possesses an obvious curvature, implying strongly that etching along many different axial orientations does exist.[24] It is very difficult to interpret the formation of these kinked structures, and hence the associated mechanisms remain unclear.

The formation of slanted wires not aligned with the $\langle 100 \rangle$ direction was also observed in our previous studies but has remained unexplained.[9,10] In this study, to verify whether the slanted wires acquired previously[9,10] are accidental, and most importantly to find out their formation mechanism, systematic chemical etchings assisted by micron-sized Au mesh were carried out at room temperature across a wide range of volume ratios R of HF acid to H_2O_2 solution. Slanted and vertical wires were observed to form in most of the parameter space and in the low-R regime, respectively. We demonstrate that a wide range of slant angles can be controllably achieved simply by tuning the volume ratio, underscoring the feasibility and appeal of this approach. The observation of R-dependent change of oxygen content in wires and bubbling phenomena is explained in the framework of two competing Si dissolution mechanisms. The slantwise mesh movement responsible for the formation of slanted wires seems to be strongly associated with a direct dissolution mechanism through hydrogen bubbles produced by this same mechanism. Bubble-induced flow was hypothesized in the end to be the probable factor enabling slanted etching.

2. Experimental details

Boron-doped p-type Si (100) wafers (nominal resistivity 1–30 Ω·cm, thickness 650–700 μm; Czochralski-grown, LG Siltron) were used. The preparation procedure and dimensions of the Au mesh are identical to those described in our previous study.[9] As-prepared meshes consist of a well-ordered hole array with a diameter of 1 μm and a center-to-center space of 2 μm. After completion of mesh preparation, the associated wafers were cut by a dicing saw into 0.5 cm×0.5 cm pieces for subsequent MACE.

The samples were etched in a mixture of 48 wt% HF acid and 30 wt% H_2O_2 (Sigma-Aldrich) solution. The volume ratio R of HF acid to H_2O_2 solution was varied over a wide range for etching, and the corresponding molar ratio provided when necessary. The etching was conducted under a stirred condition based on paddle rotation[25] unless otherwise specified (Fig. 1(a)). In all cases, the etching duration was kept relatively short to prevent ambiguity, as prolonged etching can produce a thick wire layer that acts as an effective diffusion barrier for reactants and products, thereby complicating the interpretation of results. Since the etching front is covered by a 100 nm Au film that is optically thick for visible and near-infrared light,[26] all etchings were performed in ambient light at room temperature.

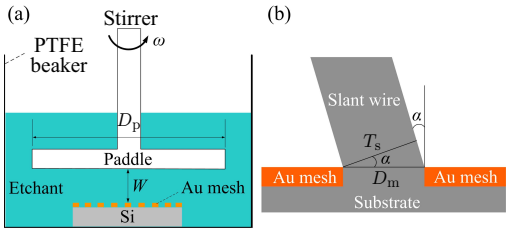


Fig. 1. Sketch of (a) etching cell setup and (b) slanted wire geometry.

Scanning electron microscopy (SEM) investigation was performed using a FEI Quanta 650 FEG microscope equipped with an INCA 350 spectrometer (Oxford Instruments) for energy dispersive x-ray spectroscopy (EDS). The nanostructures of the prepared wires were investigated by transmission electron microscopy (TEM; FEI TITAN ChemSTEM 80-200). For SEM, bird's-eye views (tilted 45°) and cross-sectional views show the overall morphology and the (110) cleavage plane of the sample, respectively. EDS was used to examine the etching-induced oxidation grade of the etched wires. To this end, a careful sample preparation procedure was implemented to minimize the influence of native oxidation and thereby more accurately reflect the oxygen content resulting from the etching process. After etching, the samples were rinsed with

deionized water and blow-dried by a nitrogen gun followed by an immediate transfer to the SEM chamber for EDS examination with a voltage of 20 kV.

Figure 1(a) shows a schematic of the etching cell setup. The paddle diameter D_p is 4 cm. The distance W between the paddle and the sample surface is set to be 4 mm unless otherwise stated. All samples are placed horizontally, and the paddle rotation speed ω is 200 revolutions per minute. In order to facilitate the discussion, Fig. 1 is drawn to define several critical geometric parameters associated with a slanted wire. $T_s = D_m \cos\alpha$, with T_s, D_m and α the thickness of the wire, the mesh diameter and the slant angle with respect to the normal of the substrate, respectively. This slant angle can be easily measured if the wire lies in the (110) plane, since this plane can be revealed by mechanical cleavage of the (100) substrate. In this work, only the wires lying in the (110) plane are used for the measurement of slant angles. If the sample does not possess wires lying in this plane for direct angle measurement, we choose to etch more samples with the same etching condition until wires lying in the (110) plane are acquired. The slant angles of wires were measured directly by a plastic protractor in cross-sectional SEM micrographs. A measurement uncertainty of $\pm 4^\circ$ was incorporated into the data analysis to account for potential misalignment of the wires from the exact (110) plane. The etch speed is calculated on the basis of the wire length measured in the (110) cleavage planes.

3. Results and discussion

To reveal the dependence of wire geometry and morphology on etchant composition, systematic etchings with a varied volume ratio of HF acid to H_2O_2 solution were carried out. Figures 2 and 3 present the results based on SEM observations (Figs. 4–6) and EDS measurements, respectively.

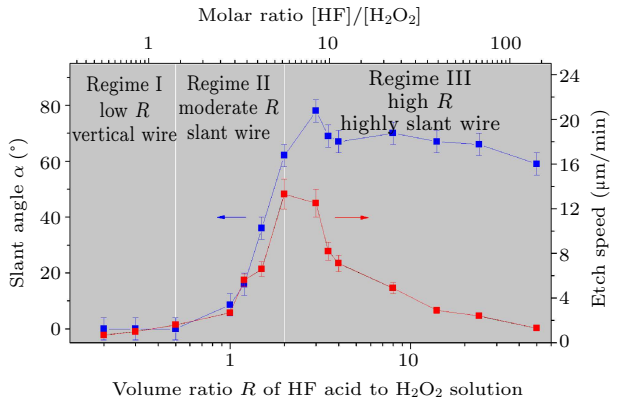


Fig. 2. The plot of slant angle α and etch speed against volume ratio R based on SEM observations. The corresponding molar ratio is also shown. The x-axis is plotted in log scale in order to present clearly the low-R regime. The lines are guides for the eye. The error bars represent measurement uncertainties of $\pm 4^\circ$ for the slant angle and $\pm 10\%$ for the etch speed. The position of the border between neighboring regimes is based on experimental results as in other works.[7,13] All data points are based on direct measurements on cross-sectional SEM images, except those for $R = 1$ which are corrected from the 45° tilt angle used by the bird's-eye view image given in Fig. S1.

In Fig. 2, the parameter space is classified into three different regimes, namely, the high-, moderate- and low-R regimes. The slant angles of the etched wires increase sharply from the low- to high-R regimes, as clearly seen in Fig. 2. Figure 3 reveals a clear negative correlation between the volume ratio R and the oxygen content of the etched wires.

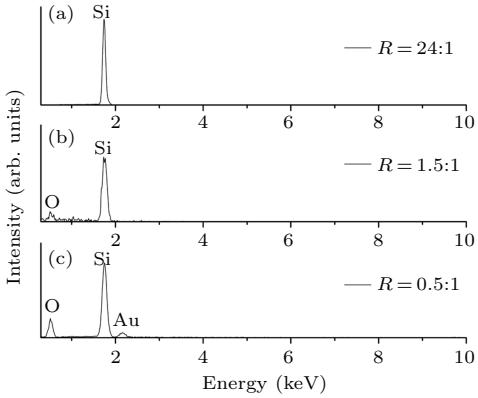


Fig. 3. The EDS results for the wires etched with a volume ratio of (a) 24:1, (b) 1.5:1 and (c) 0.5:1 representative of the high-, moderate- and low-R regimes, respectively. The atomic ratio of O to Si is ~ 0. (b) An obvious oxygen peak appears and EDS analyses give an atomic ratio of O to Si elements of 21:79. (c) Au is detected and the atomic ratio of O, Si and Au is measured by EDS to be 69:30:1.

In the high-R regime, reducing R from 50:1 to 2:1 causes the slant angle to vary non-monotonically, initially increasing from 59° to a maximum of 78° before decreasing to 62°. Basically, the slant angle varies gently with a drastically changed volume ratio. Further examinations by both highly zoomed SEM and TEM views show that the slanted wires obtained in this regime are essentially solid nanobelts (Figs. 5(a) and 5(b)) with an elliptical cross section (Fig. 5(a)) and with their surface somewhat rough at the nanoscale (Figs. 5(c)). In the moderate-R regime, etching with volume ratios of 1.5:1 (Figs. 6(a) and 6(b)), 1.2:1 (Figs. 6(c) and 6(d)) and 1:1 (Fig. S1) leads to slant angles of 36°, 16° and 8.6°, respectively. This regime features both a small oxygen peak in the EDS spectrum (Fig. 3(b)) and a drastic change of slant angle with a slightly modified volume ratio.

In contrast to the formation of slanted wires in moderate- and high-R regimes, vertical wires form only in the low-R regime (Fig. 7). Etching in an ultra-low volume ratio produces tapered wires, some exhibiting spaghetti-like morphologies while maintaining roots perpendicular to the substrate (Fig. 7(c)). Etching with a volume ratio of 0.2:1 results in the simultaneous formation of both vertical wires with a low aspect ratio and sparsely scattered craters filled with nanoporous Si (Fig. S2). These craters exactly resemble those already reported.[13] Further decreasing the volume ratio to 0.1:1 renders wire formation impossible, leading to the formation of just craters similar in morphology to the former case and to peeling-off of the metal mesh (Fig. S3). Both the formation of these craters and the peeling-off of Au mesh strongly indicate

that their associated etching is very close to the regime of electropolishing dominated by oxide formation.[7,13] The vertical wires formed in the low-R regime are actually porous (Fig. 7) with an atomic ratio of O to Si close to 2 (Fig. 3(c)). Comparing this ratio with those characteristic of moderate- and high-R domains (Figs. 3(a) and 3(b)) indicates that the formation of SiO_x species is dominant in this low-R regime. Au is detected to also be present in the vertical wires. This may be because this low-R regime features a very high $[H_2O_2]$ (Fig. 2) and thus peroxide can react intensely with Au mesh, forming many Au ions that are reduced subsequently to Au particles during MACE.[4] These Au particles are consequently responsible for the formation of both the porous wires and the craters unique to this low-R regime. Because these Au particles were trapped deeply in the porous wire and could not be rinsed out by the procedure given in section 2, we observe a small gold peak in Fig. 3(c). The mechanism related to dynamic electrochemical redistribution of precious metal during MACE can be found elsewhere.[4]

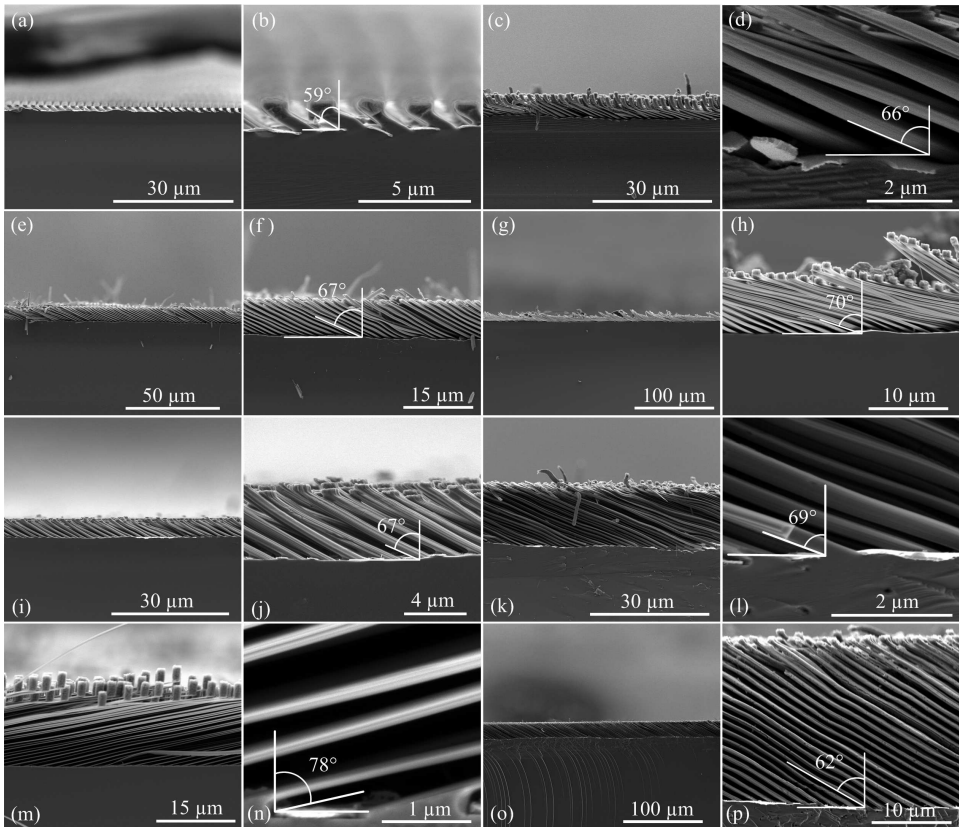


Fig. 4. Cross-sectional SEM micrographs of the wires etched with a high volume ratio: (a) and (b) $R = 50:1$ for 2 min; (c) and (d) $R = 24:1$ for 4 min; (e) and (f) $R = 14:1$ for 6 min; (g) and (h) $R = 8:1$ for 5 min; (i) and (j) $R = 4:1$ for 1.5 min; (k) and (l) $R = 3.5:1$ for 5 min; (m) and (n) $R = 3:1$ for 4 min; (o) and (p) $R = 2:1$ for 3 min. Parts (a), (c), (e), (g), (i), (k), (m) and (o) give overviews with (b), (d), (f), (h), (j) (l), (n) and (p) giving the respective zoomed views.

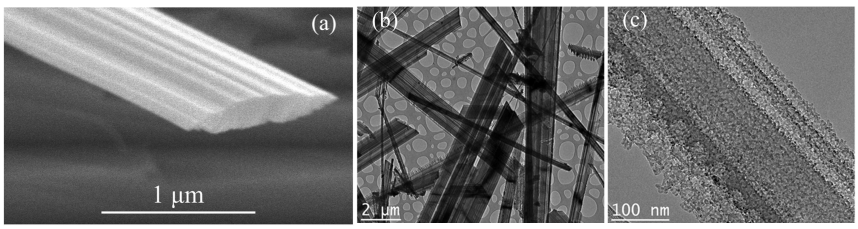


Fig. 5. Typical morphology of the slanted wires obtained in the high-R regime. (a) Zoomed-view SEM micrograph showing the solid cross-section of a single slanted wire. (b) Overview TEM micrograph showing their belt-like structures. (c) Zoomed-view TEM micrograph showing a typical wire surface that is rough at the nanoscale.

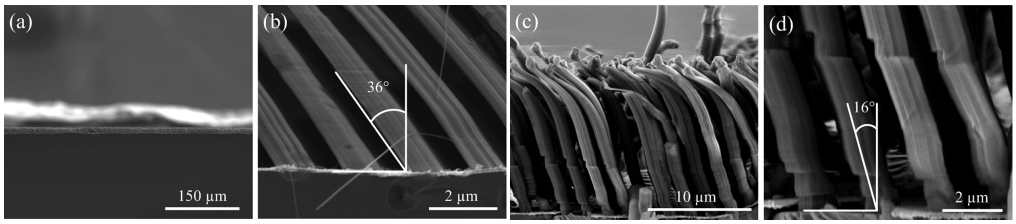


Fig. 6. Cross-sectional SEM micrographs of the wires etched with a moderate volume ratio: (a) and (b) $R = 1.5:1$ for 2 min; (c) and (d) $R = 1.2:1$ for 3 min. Parts (a) and (c) give overviews and (b) and (d) the respective zoomed views.

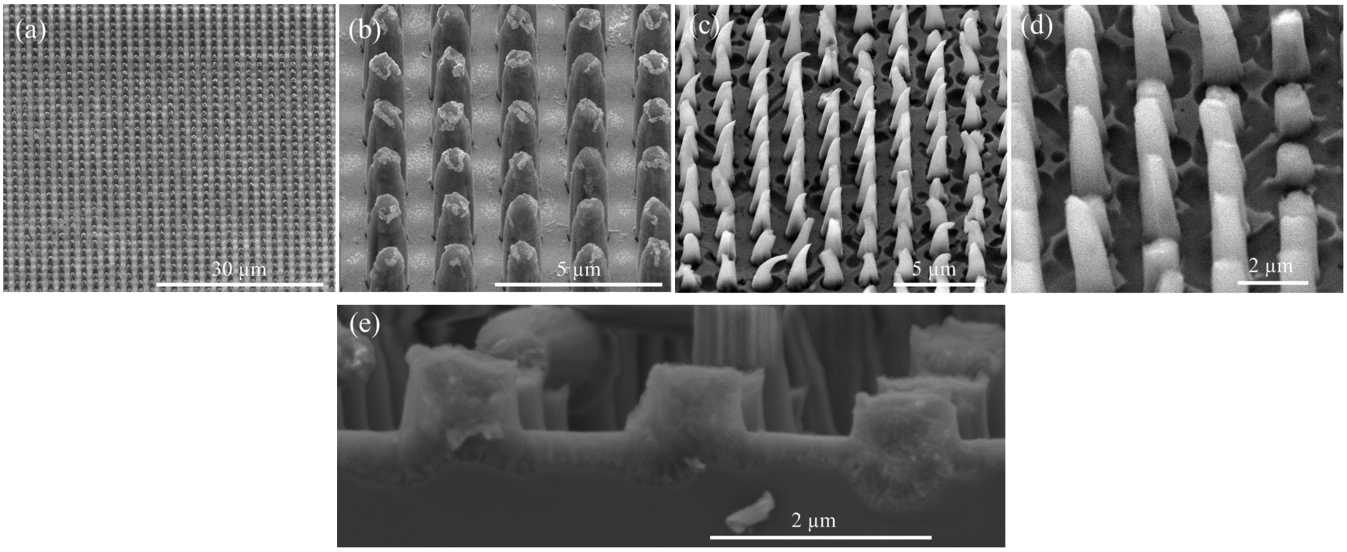


Fig. 7. SEM micrographs of the wires etched with a low volume ratio: (a) and (b) bird's-eye view SEM with $R = 0.5:1$ for 5 min; (c) and (d) bird's-eye view SEM with $R = 0.3:1$ for 2 min. Parts (a) and (c) give overviews and (b) and (d) the respective zoomed views. (e) The cross-sectional SEM micrograph ($R = 0.5:1$ for 5 min) shows that these vertical wires are actually porous. The border line between the porous and solid regions is clearly visible, and this cross section is distinctly different from those of the solid wires shown in Fig. 4 where no such border line exists.

Generally, the high-R regime is dominated by vigorous bubbling and highly tilted wires. By sharp contrast, in the low-R regime no obvious bubbling can be observed and vertical wires form. In the intermediate regime between both, slant angle increases sharply with a slightly raised volume ratio, and indeed only weak or moderate bubbling is observed. These results are summarized in Table 1.

Table 1. Comparison of the results obtained in the three different regimes.

	Regime I	Regime II	Regime III
Volume ratio R	Low	Moderate	High
Oxygen content in wires	High	Low or moderate	Negligible
Hydrogen bubbling	Not obvious	Weak or moderate	Vigorous
Slant angle α	$\sim 0^\circ$	Low or moderate	High

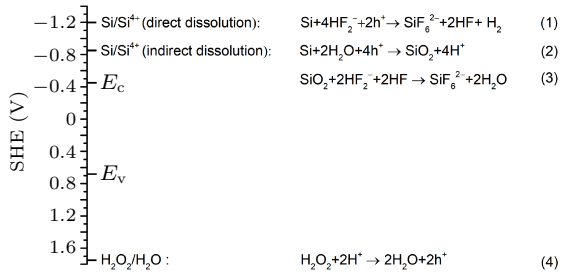


Fig. 8. Energy band diagram of Si and the standard electrode potentials of reactions involved in MACE. E_c and E_v represent the conduction and valence band edges of Si, respectively. The standard electrode potentials of anodic and cathodic reactions were based on the work of Chartier *et al.*[13] In aqueous HF solution, the anodic dissolution of Si has two principal competing paths, one via the reaction with HF (Reaction 1) and the other with H_2O (Reactions 2 and 3).[18] SHE, standard hydrogen electrode.

To rationalize the aforementioned results, we introduce the concept of current efficiency for the competing electrode reactions, which is defined as the ratio of the partial to the total current density following Bard and Vogt.[27,28] For our case, two anodic reaction paths associated with the direct and indirect dissolution of Si, respectively, compete with each other (Fig. 8).[18] The total current density equals the cathodic current density. At cathodic sites, the rate-limiting step is the generation of holes by the cathodic reaction (Reaction 4 in Fig. 8),[8,12,13] so the cathodic current density is

$$j_c = zek_c n_s c_{ox} e^{\frac{-E_a}{RT}}, \tag{1}$$

where z, e, k_c, n_s, c_{ox}, E_a, k_B and T are the number of electrons transferred during the above reaction, the charge of an electron, the rate constant, the electron density, the H_2O_2 concentration, the activation energy for the above reaction, the Boltzmann constant and the absolute temperature, respectively.[8,12,13] The partial anodic current density associated with direct mechanism (termed direct current density for the ease of discussion) is

$$j_{a,d} = j\varepsilon_d = \varepsilon_d zek_c n_s c_{ox} e^{\frac{-E_a}{RT}}, \tag{2}$$

with ε_d the current efficiency associated with direct dissolution of Si (termed direct current efficiency hereafter). Similarly, the partial anodic current density associated with indirect mechanism (termed indirect current density hereafter) is

$$j_{a,i} = j\varepsilon_i = \varepsilon_i zek_c n_s c_{ox} e^{\frac{-E_a}{RT}}, \tag{3}$$

with ε_i the current efficiency associated with indirect dissolution of Si (termed indirect current efficiency hereafter). Since

the total current density $j_c = j_{a,d} + j_{a,i}$, it is obvious that

$$\varepsilon_d + \varepsilon_i = 1. \tag{4}$$

Disappointingly, it is difficult to find in the existing literature the exact value of ε_d and/or ε_i corresponding to each volume ratio, in particular for Au-assisted etching in a solution containing HF and H_2O_2, perhaps due to the difficulty in measuring the exact amount of reaction products particularly for MACE.[13,18] However, according to the results given in Table 1, the behavior of ε_d and ε_i in the three different regimes can be estimated, at least roughly, as summarized in Table 2. Since the exact current efficiency associated with each volume ratio remains unknown, it is impossible to calculate the exact position of the border between neighboring regimes. Therefore, the regime boundaries shown in Fig. 2 are determined empirically from our experimental results, consistent with the approach adopted in earlier studies.[7,13]

Table 2. Behavior of current efficiency in three regimes based on experimental observations.

	Regime I	Regime II	Regime III
Volume ratio R	Low	Moderate	High
Direct current efficiency ε_d	Low	Depending greatly on R	High
Indirect current efficiency ε_i	High	Depending greatly on R	Low

With the above equations, the experimental results can be interpreted by the competition between two distinct mechanisms, namely the direct and indirect mechanisms associated with direct and indirect dissolution of Si atoms, respectively (Fig. 8). The direct mechanism means that Si atoms are etched away directly by HF species as shown in Reaction 1. In contrast, the indirect mechanism proceeds through two successive steps (Reactions 2 and 3).[18] That is, Si is oxidized by injected electronic holes as a first step (Reaction 2), and in the subsequent second step, Si oxides produced by Reaction 2 are removed by HF species (Reaction 3).[18] Cathodic Reaction 4 provides the total electronic holes required by anodic Reactions 1 and 2.

Two factors may be crucial to further differentiating the direct mechanism from the indirect one. First, to etch out one Si atom, the direct mechanism needs only two holes, considerably fewer than the four holes required by the indirect mechanism. Secondly, the direct mechanism is more favored in energetics compared with its indirect counterpart, as shown in Fig. 8. Figure 9 gives the energy band diagram proposed for both moderate- and high-R regimes. In these regimes, the mesh cannot contact intimately with the Si substrate due to continuous hydrogen bubble nucleation, growth, and transfer in the channel between the mesh and the substrate surface. Rather, during MACE in the moderate- and high-R regimes, the mesh should be surrounded by a two-phase fluid consisting of hydrogen bubbles and etchant (Fig. S4). Hence, an electrolyte/Si junction rather than an Au/Si one is proposed. This electrolyte/p-Si junction exhibits behavior analogous to a Schottky contact,[29] resulting in band bending similar in form but distinct in magnitude from that reported for metal/p-Si junctions.[23] At anodic sites, for low-doped Si, the current density available for the direct and indirect mechanisms depends exponentially on their potential drop in the space charge layer $\eta_{sc,d}$ and $\eta_{sc,i}$, respectively,[15,18] as dictated by the theoretical expression of current density for a Schottky-like junction.[23] This exponential dependence can also be derived from the fifth and sixth equations in Ref. [15], since for our low-doped Si the potential drop η_h in the Helmholtz layer can be assumed to be zero. Figure 9 illustrates how the direct mechanism is more energetically favored than the indirect one.

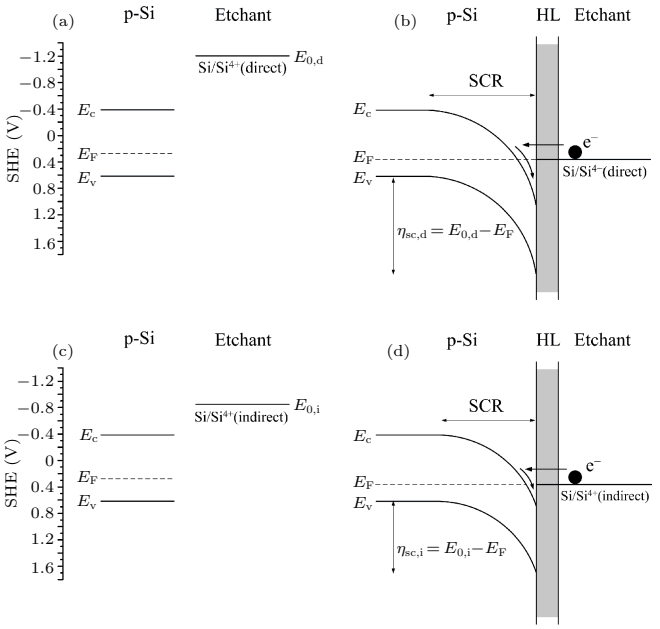


Fig. 9. The energy band diagrams at anodic sites under standard conditions proposed for both moderate- and high-R regimes: (a) and (b) direct mechanism; (c) and (d) indirect mechanism. Parts (a) and (c) are before contact between Si and etchant and (b) and (d) in equilibrium (after contact). For low-doped Si, most of the potential drops across the space-charge region (SCR), and hence the potential drop η_h in the Helmholtz layer (HL) is neglected here. In (b), since $E_{0,i} - E_{0,d} \approx 0.36$ V vs. SHE (standard hydrogen electrode),[13] the band bending η_{sc} of the direct mechanism is ~ 0.36 V greater than in (d) for the indirect mechanism, resulting in a greater charge transfer rate for direct mechanism in the SCR.[18,23]

The above two factors may be helpful for understanding the different behaviors of current efficiency in the three regimes (Table 2) and hence the overall experimental results observed in this work. In the high-R regime, due to its relatively low $[H_2O_2]$ compared with those of the other two, the total current density and hence the electronic hole den-

sity available for etching is limited (Eq. (1)). Meanwhile, in this region [HF] is quite high. The combined conditions of low [H_2O_2], high [HF] and the exclusive energetic favorability of the direct mechanism (Fig. 9) prevent the accumulation of excess holes required for indirect Si dissolution. Finally, a high direct current efficiency is reached, and in turn the direct mechanism dominates this high-R region. Consequently, we observed vigorous hydrogen bubbling and no oxygen peak in EDS. By stark contrast, in the low-R regime, since [H_2O_2] is much higher than [HF], excess electronic holes are afforded ample opportunity to accumulate at the etching front and to oxidize the Si surface before HF species are available, rendering a high indirect current efficiency. As a result, the indirect mechanism dominates this low-R region: there was no obvious bubbling and a high oxygen content in the wires was evidenced. Actually, the atomic ratio of O to Si elements is detected on all vertical wires by EDS to be very close to 2:1 (Fig. 3(c)), indicating that this low-R regime is dominated by Reaction 2 in Fig. 8. The observation of both crater formation and peeling-off of mesh in this regime (Figs. S2 and S3) further confirms the above conclusion,[7,13] since the formation of craters indicates that their associated etchings are very close to the regime of electropolishing with its indirect current efficiency equal to ~ 1.[13] The peeling-off of mesh was also attributed to the dominance of oxide formation.[7] During etching, the surface oxides on these vertical wires are continuously — though slowly — removed by the limited amount of HF species available in this low-R regime. Hence wire tapering was observed (Fig. 7). In the intermediate regime, compared with the other two, both [H_2O_2] and [HF] are moderate. As a result, both mechanisms play a role, producing both hydrogen and oxides. The atomic ratio of O to Si elements of 0.27 observed in this intermediate regime (Fig. 3(b)) also supports this conclusion, since this atomic ratio is obviously lower than that (~ 2) detected in the low-R region.

The observed variation of etch speed with volume ratio (Fig. 2) can also be interpreted in the framework of two competing mechanisms. In the high-R regime, the etch speeds range from 2 μm/min to 15 μm/min, much faster than those (no more than 1 μm/min) speeds observed in the low-R region. This difference arises from two concurrent factors: (i) the significantly higher indirect current density in the low-R regime, driven by elevated [H_2O_2] and ε_i (Eq. (3)), directs most current toward oxide formation; (ii) simultaneously, the considerably lower [HF] in this regime substantially retards the dissolution of the formed oxide. For instance, dissolving the oxide layer generated by each cycle of its associated current bursts can take as long as ~ 100 s, as revealed clearly by the measured chronopotentiometric curve.[30] The rapid increase of etch speed with R observed in the moderate region is due to the decrease of both [H_2O_2] and ε_i, as well as to the increase of [HF], resulting in both the formation of fewer oxides and their quicker dissolution in HF solution. In the high-R region, the decrease of etch speed with an increasing volume ratio can be attributed mainly to the decrease of direct current density with decreasing [H_2O_2], as suggested by Eq. (2).

One last question remains: what is responsible for the formation of slanted wires? The wide variation in slant angles, which shows no preferred crystallographic orientation (Fig. 2), challenges existing theoretical frameworks in explaining their formation at room temperature. Slanted wires were produced in the majority of the parameter space explored. Only etching with a very low volume ratio enabled vertical wire formation. Extensive etchings with a widely varied R suggested that slanted wires always and only form in the moderate- and high-R regimes. Most importantly, slant angles in the high-R regime are generally greater than those in the moderate-R regime. All these observations imply that there might be a close correlation between the direct mechanism and the formation of slanted wires. But the direct mechanism itself cannot explain directly why the mesh moves slantwise during MACE. Undoubtedly it is this slantwise movement of mesh that drives the slantwise etching and hence the formation of slanted wires. A search of the literature reveals that bubbling, or to be more exact the bubble-induced flow and its associated hydrodynamic force acting on the Au mesh, might be the key to understanding this slantwise movement.[27,28,34] As mentioned before, during MACE the mesh is actually surrounded by a two-phase fluid consisting of hydrogen bubbles and etchant. Hence there exist ample opportunities for hydrodynamics (Fig. S4). Actually, from a viewpoint of fluid mechanics, our Au mesh is a thin plate with both its overall size and its Reynolds number comparable to those of insect wings studied in our previous works.[35–38] Thus it would be expected that the fluid-mechanical behavior of our mesh should be sensible to small flow perturbations similar to the insect wing case.[35,36] In this sense, the hydrogen bubble-induced flow has the potential to drive the mesh slantwise in a hydrodynamic manner.[39,40] However, verification of this assumption requires flow visualization, which is usually achieved by means of particle image velocimetry (PIV).[34] However, during MACE the dense wire arrays obstruct the optical path required for PIV, which must be aligned parallel to the substrate to visualize the flow structures. As a result, it would be fairly difficult to visualize the flow velocity field around the mesh localized at the etching front, making it impossible to easily verify the above hypotheses at the moment.

Anyway, this work implies strongly that the slant angle can be tuned over a wide range simply by adjusting the volume ratio (Fig. 2). Since these wire arrays are well-ordered in a large scale (Fig. 10) with a controllable slant angle, they can function well as excellent building blocks for a wide

spectrum of applications, for example in the field of energy conversion.[41–46] Furthermore, this study establishes a foundation for controllable pore formation via MACE.[44]

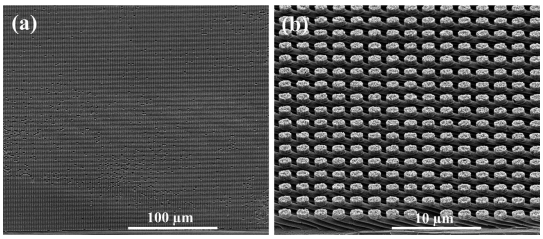


Fig. 10. Bird's-eye view SEM micrographs of wires etched with $R = 24:1$ for 5 min: (a) overview and (b) zoomed view.

4. Conclusion

P-type (100) Si samples were etched by MACE across a wide range of volume ratios R of HF acid to H_2O_2 solution. Slanted wires formed in the parameter space with a moderate and high R, whereas vertical wires formed only in the low-R regime. The wide variation in slant angles indicates the absence of a preferred crystallographic etching direction in the associated MACE processes. A change of bubbling phenomena and oxygen content in wires with volume ratio was observed and explained by the competition between the mechanisms associated with direct and indirect Si dissolution. Obviously, the formation of slanted wires is caused directly by slantwise mesh movement. While this movement seems to be closely associated with the direct mechanism, it cannot be interpreted directly by this same mechanism. We propose that bubble-induced flow can hydrodynamically drive the slantwise movement of the mesh, thereby directly facilitating the formation of slanted wires.

Acknowledgements

This study was supported by the Startup Fund for Introduced Talents of Nanjing University of Information Science and Technology, the National Key Research and Development Program of China (Grant No. 2023YFF0713303) and the Jiangsu Provincial Frontier Technology Research and Development Plan (Grant No. BF2024030).

References

[1] Hildreth O and Wong C P 2016 *Materials for Advanced Packaging* (Cham: Springer) pp. 879–922
[2] Huo C, Wang J, Fu H, Li X, Yang Y, Wang H and Peng K Q 2020 *Adv. Funct. Mater.* **30** 2005744
[3] Han H, Huang Z and Lee W 2014 *Nano Today* **9** 271
[4] Smith Z R, Smith R L and Collins S D 2013 *Electrochim. Acta* **92** 139
[5] Huang Z, Geyer N, Werner P, De Boor J and Gösele U 2011 *Adv. Mater.* **23** 285
[6] Liu L and Bao X Q 2014 *Mater. Lett.* **125** 28
[7] Kim J, Han H, Kim Y H, Choi S H, Kim J C and Lee W 2011 *ACS Nano* **5** 3222
[8] Kim J, Kim Y H, Choi S H and Lee W 2011 *ACS Nano* **5** 5242
[9] Bao X Q, Ferreira R, Paz E, Leitao D C, Silva A, Cardoso S and Liu L 2014 *Nanoscale* **6** 2097
[10] Bao X Q and Liu L 2014 *J. Power Sources* **268** 677
[11] Matsumoto A, Son H, Eguchi M, Iwamoto K, Shimada Y, Furukawa K and Yae S 2020 *RSC Adv.* **10** 253
[12] Gondek C, Lippold M, Röver I, Bohmhammel K and Kroke E 2014 *J. Phys. Chem. C* **118** 2044
[13] Chartier C, Bastide S and Lévy-Clément C 2008 *Electrochim. Acta* **53** 5509
[14] Kolasinski K W 2009 *Surf. Sci.* **603** 1904
[15] Bertagna V, Plougonven C, Rouelle F and Chemla M 1996 *J. Electrochem. Soc.* **143** 3532
[16] Li X and Bohn P W 2000 *Appl. Phys. Lett.* **77** 2572
[17] Lehmann V 2002 *Electrochemistry of Silicon: Instrumentation, Science, Materials and Applications* (Weinheim: Wiley-VCH)
[18] Zhang G X 2006 *In Modern Aspects of Electrochemistry* (Boston: Springer) pp. 65–133
[19] Lehmann V and Föll H 1990 *J. Electrochem. Soc.* **137** 653
[20] Huang Z, Shimizu T, Senz S, Zhang Z, Geyer N and Gosele U 2010 *J. Phys. Chem. C* **114** 10683
[21] Chen H, Wang H, Zhang X H, Lee C S and Lee S T 2010 *Nano Lett.* **10** 864
[22] Chen Y, Zhang C, Li L, Tuan C C, Wu F, Chen X and Wong C P 2017 *Nano Lett.* **17** 4304
[23] Lai R A, Hymel T M, Narasimhan V K and Cui Y 2016 *ACS Appl. Mater. Interfaces* **8** 8875
[24] Sandu G, Avila Osses J, Luciano M, Caina D, Stopin A, Bonifazi D and Ersen O 2019 *Nano Lett.* **19** 7681
[25] Kralj B and Dryfe R A 2003 *Electrochem. Commun.* **5** 325
[26] Genet C and Ebbesen T W 2007 *Nature* **445** 39
[27] Bard A J and Faulkner L R 2001 *Electrochemical Methods: Fundamentals and Applications* 2nd edn. (New York: Wiley)
[28] Vogt H 1984 *Electrochim. Acta* **29** 167
[29] Quiroga-González E and Föll H 2016 *In Porous Silicon: From Formation to Application: Formation and Properties*, Volume One (Boca Raton: CRC Press) pp. 46–63
[30] Foca E, Carstensen J and Föll H 2007 *J. Electroanal. Chem.* **603** 175
[31] Föll H, Leisner M, Cojocaru A and Carstensen J 2009 *Electrochim. Acta* **55** 327
[32] Föll H, Langa S, Carstensen J, Christophersen M and Tiginyanu I M 2003 *Adv. Mater.* **15** 183
[33] Föll H and Carstensen J 2011 *J. Electrochem. Soc.* **158** D357
[34] Yang X, Karnbach F, Uhlemann M, Odenbach S and Eckert K 2015 *Langmuir* **31** 8184
[35] Bao X Q, Vanneste T, Bontemps A, Grondel S, Paquet J B and Cattan E 2011 2011 *IEEE International Conference on Robotics and Biomimetics* (Piscataway: IEEE) pp. 1487–1494
[36] Vanneste T, Paquet J B, Bao X Q, Dargent T, Grondel S and Cattan E 2010 *International Micro Air Vehicle Conference and Flight Competition (IMAV)*
[37] Bao X Q, Bontemps A, Grondel S and Cattan E 2011 *J. Micromech. Microeng.* **21** 125020
[38] Dargent T, Bao X Q, Grondel S, Le Brun G, Paquet J B, Soyer C and Cattan E 2009 *J. Micromech. Microeng.* **19** 085028
[39] Jones A M and Knudsen J G 1961 *AIChE J.* **7** 20
[40] Pezzulla M, Strong E F, Gallaire F and Reis P M 2020 *Phys. Rev. Fluids* **5** 084103
[41] Li X 2012 *Curr. Opin. Solid State Mater. Sci.* **16** 71
[42] Carbó-Argibay E, Bao X Q, Rodríguez-Abreu C, Cerqueira M F, Petrovykh D Y, Liu L and Kolen'ko Y V 2015 *J. Colloid Interface Sci.* **456** 219
[43] Bao X Q and Liu L F 2015 *Mater. Chem. Phys.* **149** 309
[44] Bao X Q, Jiao J W, Zhou J and Wang Y L 2007 *Electrochim. Acta* **52** 6728
[45] Chen X, Wang Y, Chen W, Zhang K, Lin Y, Li H and Liu Z 2023 *Chin. Phys. B* **33** 018801
[46] Liu Z, Du L, Zhang S H, Cai J, Meng F and Li Z 2023 *Chin. Phys. B* **32** 020701